

Controllable hydro-thermoelastic heat transport in ultrathin semiconductors at room temperature

Received: 30 June 2025

Accepted: 16 April 2026

Published online: 15 May 2026

 Check for updates

S. Varghese^{1,2}, J. Tur-Prats³, J. D. Mehew¹, D. Saleta Reig^{1,2}, R. Farris¹, J. Camacho³, J. A. Haibeh⁴, A. Sokolov^{4,5}, P. Ordejón¹, S. Huberman⁴, A. Beardo^{3,6}, F. X. Alvarez³ & K. J. Tielrooij^{1,2}✉

Heat flow in semiconductors typically occurs through the diffusive transport of lattice vibrations. Non-diffusive hydrodynamic effects associated with viscous heat flow and thermoelastic effects—in which heat changes the interatomic spacing in the lattice—can affect heat conduction. However, the interplay between hydrodynamic and thermoelastic effects on heat transport has so far been overlooked. Furthermore, unconventional thermoelastic effects due to inhomogeneous strain fields at the nanoscale have so far not been observed experimentally. Here we show that the combination of hydrodynamic and thermoelastic effects leads to a highly non-diffusive hydro-thermoelastic heat transport regime with a controllable reduction in the effective thermal diffusivity for two-dimensional semiconductors. We observe this in MoSe₂ and MoS₂ through real-space heat tracking with nanometre spatial accuracy using spatiotemporal pump–probe thermometry. Our experiments are conducted at room temperature and demonstrate control through the thickness of the material and by choosing continuous or pulsed heating. Our model of hydro-thermoelastic heat transport, based on atomistic input parameters, reproduces the experimental observations and identifies the occurrence of a counterintuitive thermoelastic heat flux contribution from cold to hot regions.

Lattice heat is carried by phonons through diffusive and non-diffusive mechanisms. Diffusive heat transport is the most common and is macroscopically described by Fourier's law¹, whereas it is microscopically governed by momentum-non-conserving phonon–phonon scattering events. Non-diffusive heat transport can involve ballistic phonon motion, first described by Casimir². In the ballistic transport regime, phonon scattering occurs at system boundaries, when system dimensions are smaller than phonon mean-free paths. A second non-diffusive heat transport regime involves hydrodynamic phonon transport, which

generally results from the slow relaxation of heat flux relative to the length scales and timescales of the experiment or system^{3,4}. This corresponds to viscous transport and is amplified at temperatures below room temperature. Observed signatures of hydrodynamic heat transport include wave-like propagation of heat known as second sound in helium⁵, bismuth⁶, sodium fluoride⁷, strontium titanate⁸, graphite⁹ and germanium¹⁰; a so-called Knudsen minimum in black phosphorous¹¹; and Poiseuille flow in quasi-one-dimensional single crystals¹², strontium titanate¹³ and graphite^{14,15}. Moreover, hydrodynamic heat transport

¹Catalan Institute of Nanoscience and Nanotechnology (ICN2), BIST & CSIC, Campus UAB, Bellaterra (Barcelona), Spain. ²Eindhoven University of Technology, Eindhoven, the Netherlands. ³Departament de Física, Universitat Autònoma de Barcelona, Bellaterra, Spain. ⁴Department of Chemical Engineering, McGill University, Montreal, Quebec, Canada. ⁵Institute of Mechanics, Technische Universität Berlin, Berlin, Germany. ⁶Department of Physics, JILA, and STROBE NSF Science and Technology Center, University of Colorado and NIST, Boulder, CO, USA. ✉e-mail: k.j.tielrooij@tue.nl

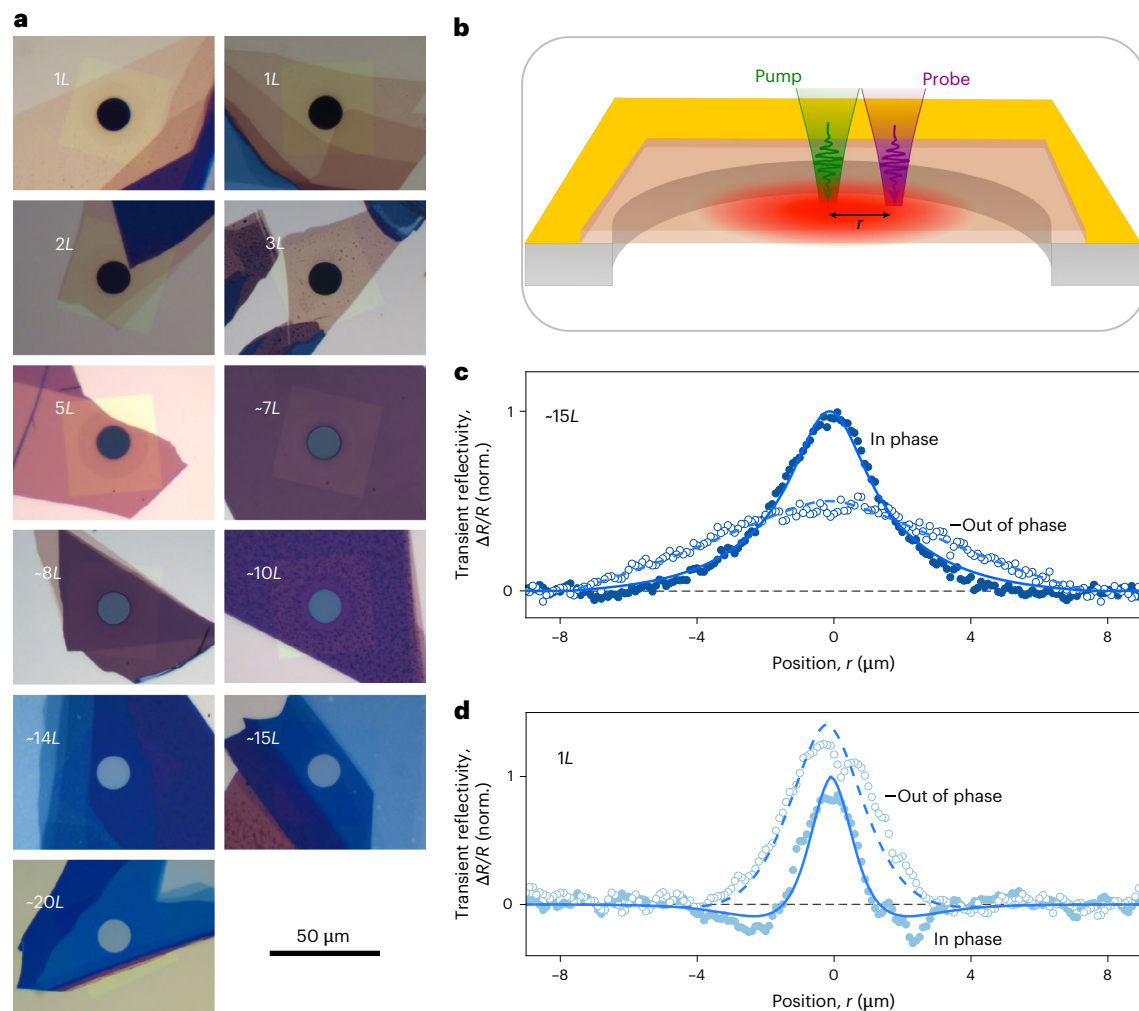


Fig. 1 | Spatiotemporally mapped heat transport in MoSe₂ crystals. a, Optical images of suspended MoSe₂ samples with the thickness given in the number of layers L . **b**, Concept of a spatiotemporal thermometry experiment in which a train of ultrafast pump pulses (green) creates a local hotspot in the centre of a suspended thin film. By spatially scanning a train of ultrafast probe pulses (purple) across the suspended region, arriving with a pump–probe delay time of ~ 13 ns, we directly track how in-plane heat flow occurs in space and time.

c,d, In-phase (filled circles) and out-of-phase (open circles) transient reflectivity profiles $\Delta R/R(r)$, normalized to the peak of the fit of the in-phase signal, measured on an ~ 15 -layer-thick (**c**) and ~ 1 -layer-thick (**d**) MoSe₂ flake. The dashed and solid blue lines correspond to a simulation of purely diffusive heat transport according to Fourier's law with the 'effective diffusivity' as an adjustable parameter (see the 'Phenomenological diffusive Fourier model' section). norm., normalized.

phenomena have been found through device heat mapping combined with mesoscopic transport models in alloys¹⁶ and silicon^{17,18}. Theoretical predictions suggested the existence of phonon hydrodynamic behaviour in two-dimensional transition metal dichalcogenide (TMD) material MoS₂ possibly up to room temperature¹⁹. However, so far, no signatures of hydrodynamic transport have been observed in TMDs at any temperature. Furthermore, thermoelastic effects have been overlooked in studies of non-diffusive heat transport. In particular, unconventional thermoelastic effects, which arise from inhomogeneous strain fields at the nanoscale, have been predicted²⁰, but they have never been observed experimentally.

Here we use spatiotemporal pump–probe thermometry²¹ to visualize heat transport in suspended large-area crystals of MoSe₂ and MoS₂ directly in real space with beyond-diffraction-limited spatial resolution. We explain the experimental results with a fit-parameter-free mesoscopic model that uses *ab initio* input parameters for its thermal properties. This combined experimental–theoretical approach reveals a thickness-controlled transition from the conventional Fourier diffusion regime in the case of relatively thick crystals to a strongly non-diffusive regime for the thinnest crystals. We attribute this transition to the interplay between non-local phonon interactions,

associated with hydrodynamic behaviour, and thermoelastic effects. In this non-diffusive 'hydro-thermoelastic' heat transport regime, pulsed heating leads to an inhomogeneous strain field that gives rise to an unconventional thermoelastic heat flux contribution from cold to hot regions, resulting in a reduction in the effective thermal diffusivity, or conductivity, by up to an order of magnitude: from 39 to 3.5 W m⁻¹ K⁻¹ for MoSe₂. Importantly, our results introduce an intrinsic and fabrication-free way to control heat transport in two-dimensional semiconductors. Thus, in addition to recently demonstrated extrinsic ways to impede thermal transport in these materials, for example, through stacking multiple layers at different twist angles²² or material patterning into phononic crystals²³, our results introduce intrinsic and active control of heat flow.

Diffusive and hydrodynamic heat transport

We prepared MoSe₂ and MoS₂ crystals with thicknesses ranging from ~ 20 layers ($20L$) to the monolayer ($1L$) limit (Fig. 1a and Extended Data Fig. 1). These crystals were suspended over a circular hole with a diameter of 15 μm to avoid substrate effects on heat transport. We perform the real-space tracking of heat flow in these samples using spatiotemporal pump–probe thermometry, where pump pulses heat the centre of a

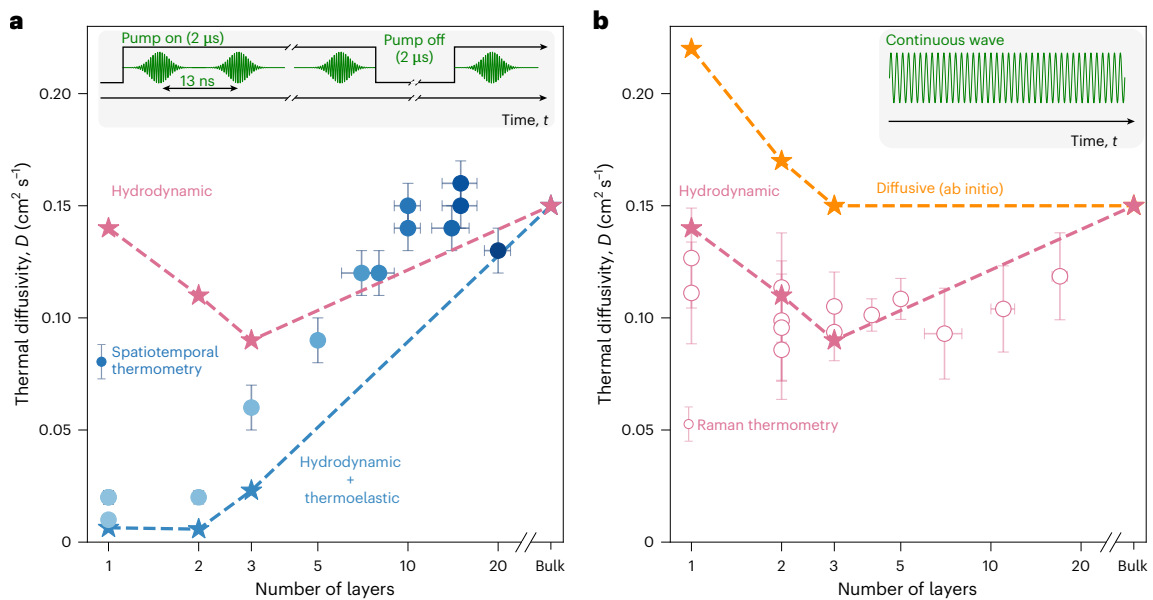


Fig. 2 | Heat transport in MoSe₂ crystals with varying thickness. a, Effective thermal diffusivities for MoSe₂ obtained using spatiotemporal pump–probe thermometry (blue closed circles), together with calculated values for hydrodynamic transport (pink stars and dashed line) and for transport that includes both hydrodynamic and thermoelastic effects (blue stars and dashed line). The inset indicates that heating occurs via modulated optical excitation. The vertical error bars indicate the uncertainty in the obtained effective thermal diffusivity D (68% confidence interval), obtained from least-squares fitting of the experimental spatial profile to the phenomenological diffusive Fourier model. The horizontal error bars indicate the uncertainty in the flake thickness

measurement. For this type of heating, the experiment shows agreement with the calculation for hydro-thermoelastic transport. **b**, Effective thermal diffusivities for MoSe₂ obtained using Raman thermometry (open circles; ref. 24), together with the calculated values for purely diffusive transport (orange stars and dashed line) and for hydrodynamic transport (pink stars and dashed line). The inset indicates that heating occurs via continuous-wave optical excitation. The vertical error bars represent the 68% confidence interval reported in ref. 24, and the horizontal error bars indicate the uncertainty in the flake thickness measurement reported in the same reference. For this type of heating, the experiment shows agreement with the calculation of hydrodynamic transport.

suspended crystal, and probe pulses spatially map out how far the heat spreads. Specifically, we record the pump-induced change in reflectivity $\Delta R/R$ as a function of pump–probe distance r with a pump–probe delay time of ~ 13 ns (Fig. 1b). We obtain both in- and out-of-phase spatial profiles, because we modulate the pump beam faster than the system returns to thermal equilibrium. Because the reflectivity is temperature dependent, the spatial profiles provide direct access to thermal diffusivity. For details on the experimental technique and extracting the thermal diffusivity, see the ‘Experimental details’, ‘Phenomenological diffusive Fourier model’ and ‘Describing in-phase and out-of-phase signals’ sections, Extended Data Figs. 3–6 and ref. 21.

Figure 1c shows an example measurement for an ~ 15 -layer-thick MoSe₂ sample, together with a simulation based on purely diffusive heat transport. The simulation describes the spatiotemporal evolution of the temperature profile using Fourier’s law and includes the lock-in operation. By simultaneously describing the in- and out-of-phase experimental profiles, we obtain a diffusivity D of 0.15 ± 0.01 cm² s^{−1} for the 15L MoSe₂ sample. This diffusivity corresponds to a thermal conductivity of ~ 28 W m^{−1} K^{−1}, and agrees well with both experimental^{24,25} and ab initio theoretical²⁶ studies of in-plane heat transport in this material. We perform spatiotemporal pump–probe thermometry measurements and simulations of purely diffusive heat transport for all different thicknesses and find that the spatial profiles for crystals with a thickness greater than three layers look qualitatively similar (Extended Data Fig. 7).

Surprisingly, for monolayer MoSe₂, we find that the spatial profile looks drastically different: much narrower and with a stronger out-of-phase signal than the in-phase signal (Fig. 1d). This suggests a strongly decreased diffusivity. Indeed, for the thinnest MoSe₂ samples, the extracted thermal diffusivities from our pump–probe measurements are about an order of magnitude lower than for thicker MoSe₂ samples (Fig. 2a). They are also much lower than the diffusivities

Table 1 | Hydro-thermoelastic model properties for MoSe₂

	Monolayer	Bilayer	Trilayer	Bulk	Reference
ρ (kg m ^{−3})	6,900	6,900	6,900	6,900	32
α (K ^{−1})	9.3×10^{-5}	7.7×10^{-5}	6.5×10^{-5}	0.7×10^{-5}	30
E (GPa)	100	130	135	165	33
ν	0.23	0.23	0.23	0.23	34
C_v (MJ m ^{−3} K ^{−1})	1.75	1.75	1.75	1.87	Ab initio
κ (W m ^{−1} K ^{−1})	39	30	26	27.5	Ab initio
τ (ps)	754	712	282	186	Ab initio
l (nm)	700	700	700	100	Supplementary Note 1
b	0.537	0.487	0.475	0.433	Ab initio

For bilayer and trilayer systems, we use a coefficient of thermal expansion α slightly increased with respect to the literature value. The Young modulus for the monolayer is extrapolated based on the findings in ref. 33.

obtained by Raman thermometry²⁴ and much lower than the diffusivities predicted by the ab initio calculations of purely diffusive heat transport for these thicknesses (Fig. 2b and Table 1). The fact that the Raman and spatiotemporal techniques have similar spot sizes but give substantially different diffusivities points to mechanisms that are beyond the conventional size effect. We will show that this is the result of non-diffusive heat transport. The extracted diffusivities are, therefore, effective diffusivities that are not necessarily associated with diffusive heat transport. Examining the spatial profiles for the thinnest MoSe₂ crystals, we observe notably narrower spatial profiles compared with thicker MoSe₂ flakes (Fig. 3a–c). We observe the same trend for MoS₂ (Fig. 3d–f). In addition, the in-phase component of the transient reflectivity signal changes sign around 2 μ m away from the photoexcited hotspot for mono- and bilayer MoSe₂ and MoS₂, whereas

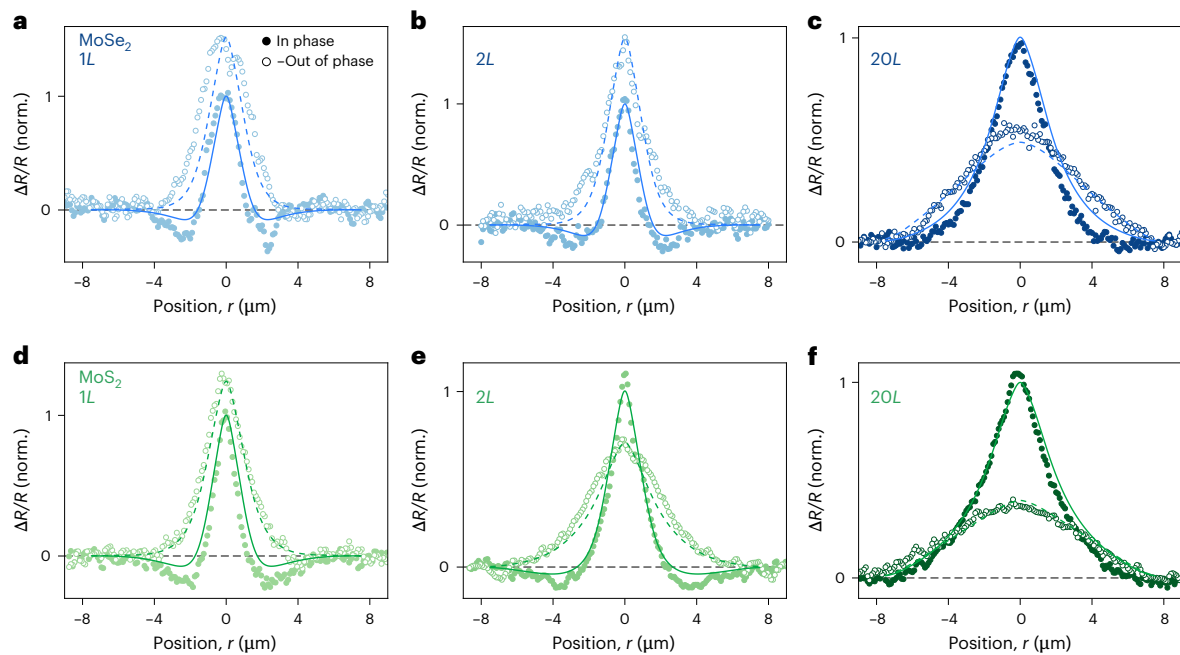


Fig. 3 | Experimental observation of strongly impeded heat transport explained by hydro-thermoelastic transport model. **a–f**, In-phase (filled circles) and out-of-phase (open circles) transient reflectivity profiles, measured on monolayer (**a**), bilayer (**b**) and 20L-thick (**c**) MoSe₂ crystals and on monolayer (**d**), bilayer (**e**) and 20L-thick (**f**) MoS₂ crystals. The emergence of a much narrower profile and a sign change around 2 μm for ultrathin crystals indicates a transition to heat transport with a strongly reduced (effective) diffusivity.

The solid and dashed lines represent the calculated spatial profiles for the in-phase and out-of-phase signals according to our mesoscopic model of hydro-thermoelastic transport (details in the main text), respectively. The profiles are normalized to the peak of the fit of the in-phase signal, and the out-of-phase profiles are multiplied by -1 . These profiles are convoluted with the probe beam spot size for a direct comparison with the experiments.

the out-of-phase signals become relatively larger. These effects are the consequence of the ultralow effective diffusivity in the thin crystals (see the ‘Describing in-phase and out-of-phase signals’ section and Extended Data Fig. 4).

Since these very low effective thermal diffusivities suggest viscous heat flow, we examine if the Guyer–Krumhansl hydrodynamic heat equation^{27,28} can reproduce the experimental results:

$$\mathbf{q} + \tau \frac{\partial \mathbf{q}}{\partial t} + \kappa \nabla T = \ell^2 \nabla^2 \mathbf{q}, \quad (1)$$

where \mathbf{q} is the heat flux vector, τ is the heat flux relaxation time, κ is the bulk in-plane thermal conductivity and ℓ is the non-local length. This equation is a generalization of Fourier’s law, including memory effects described by the second term on the left side and non-local (viscous) effects described by the term on the right side. We solve this equation along with the energy balance equation including the heat source using finite elements²⁹ with isothermal boundary conditions at the edges of the system (see the ‘DFT input for the mesoscopic model’ section and Supplementary Note 1). We first solve the equation without considering non-local and memory effects (Fig. 4a). The result reflects conventional diffusive behaviour, and both in-phase and out-of-phase profiles quantitatively agree with the measured spatial profile for the thick sample (Fig. 3c,f), where we use the thermal conductivity κ as obtained from ab initio calculations (Tables 1 and 2).

Importantly, purely diffusive transport would lead to an increase in diffusivity towards thinner crystals, which is incompatible with the experimental observations by both Raman thermometry and spatiotemporal pump–probe thermometry (Fig. 2a,b). When we include non-local and memory effects, using τ from ab initio input and limiting ℓ to the size of the initial hotspot, the profile becomes narrower, which reflects the viscous behaviour of hydrodynamic heat transport. The effective diffusivities that we extract from these profiles are in agreement with the experimentally obtained values using Raman

thermometry (Fig. 2b). This provides a key insight, that is, hydrodynamic effects play a non-negligible role in room-temperature heat transport in these TMDs. Specifically, the experimentally obtained diffusivity for monolayer MoSe₂ from Raman thermometry is $\sim 40\%$ lower than the one predicted by diffusive transport. Our mesoscopic model, which accounts for hydrodynamic effects, predicts a similar decrease in effective diffusivity.

To further confirm the effect of hydrodynamic heat transport, we use an independent theoretical approach, where we solve the linearized Boltzmann transport equation (LBTE) with ab initio inputs for monolayer MoSe₂ at 300 K, including non-diffusive effects and considering a thermal excitation that corresponds to the experimental pump spot size (see the ‘DFT details for LBTE calculations’ section). These calculations yield an effective diffusivity that is 10%–30% lower than the value expected for diffusive transport (Extended Data Fig. 8), confirming the presence of a significant hydrodynamic effect in these materials at room temperature. We, thus, find experimental signatures that confirm previous theoretical predictions of hydrodynamic heat transport in MoS₂ at room temperature¹⁹.

Combined hydrodynamic and thermoelastic effects on heat transport

Having established the significant role of hydrodynamic effects on heat transport in ultrathin MoSe₂ and MoS₂, we now focus on understanding the strong reduction in the effective diffusivity observed for the thinnest crystals under pulsed heating. We find that hydrodynamic effects alone are not sufficient to explain the experimental observations using spatiotemporal pump–probe thermometry (Extended Data Fig. 9a). To address this, we realize that photoinduced heating leads to thermal expansion inside the initial hotspot and compression further away. In addition, we realize that the thinnest crystals display a larger coefficient of expansion than the thicker crystals³⁰. Interestingly, considering diffusive heat transport in combination with conventional thermoelastic

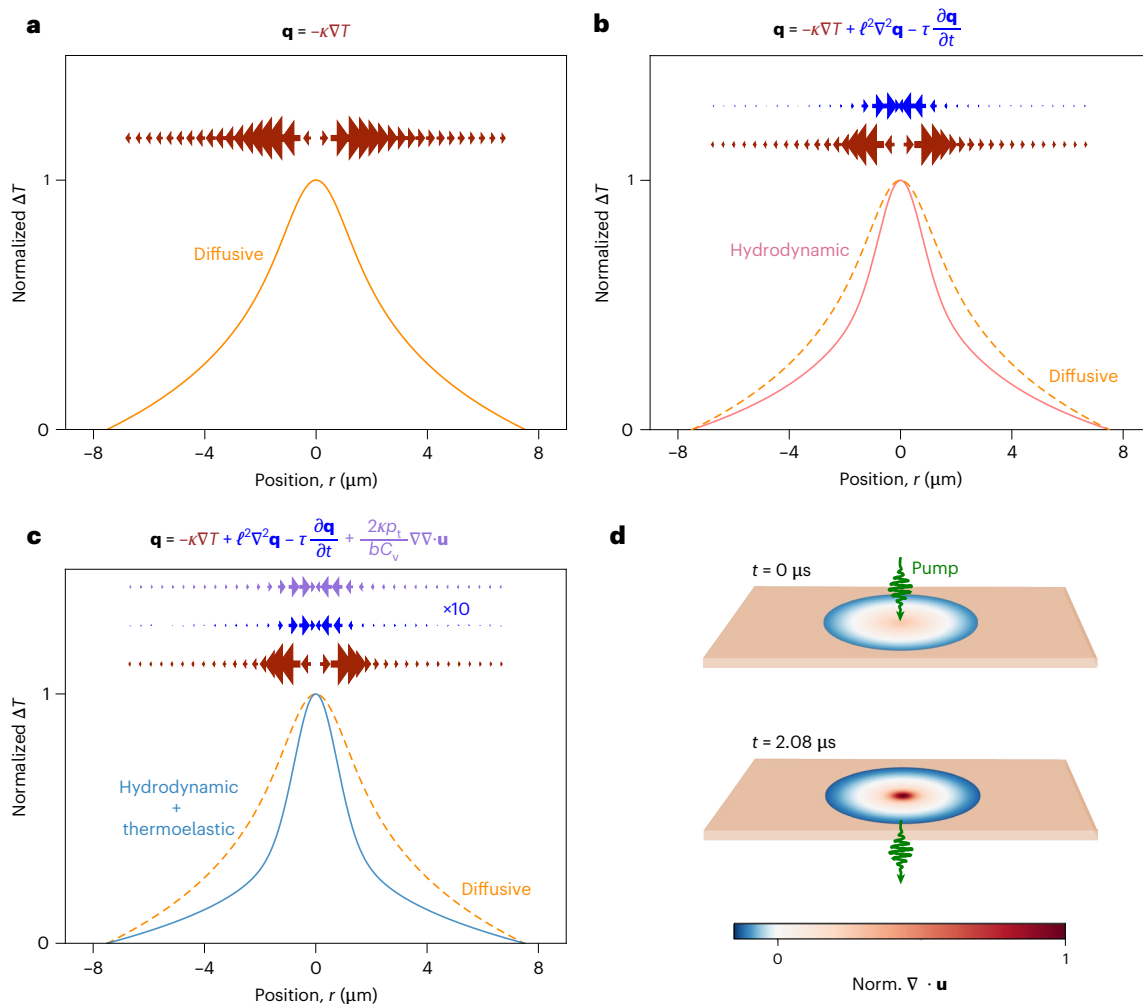


Fig. 4 | Diffusive and non-diffusive contributions to heat transport.

a–c. Calculated temperature profiles at the end of a pump-on window from the transport equation for the diffusive (**a**), hydrodynamic (**b**) and hydrothermoelastic (**c**) regimes, with the diffusive profile for comparison, together with arrows whose size reflects the strength and direction of the heat flux

contribution according to the diffusive (brown arrows), hydrodynamic (blue arrows) and thermoelastic (purple arrows) terms. **d.** Calculation of the spatially dependent divergence of the displacement vector (normalized), which represents the normalized change in density due to strain during a pump-on window. The centre region is expanded, whereas the edge is compressed.

effects, specifically accounting for thermal expansion and thermo-mechanical energy exchange, gives a spatial profile that is just a bit narrower than the purely diffusive profile (Extended Data Fig. 9b). Thus, conventional thermoelastic effects alone cannot explain the experimental observations.

We, therefore, consider the combination of hydrodynamic and thermoelastic effects induced by an inhomogeneous strain field at the nanoscale, specifically the emergence of inhomogeneous phonon dispersion relations and a modification of local phonon distributions^{20,27}. As discussed in Supplementary Note 1, these two thermoelastic effects cancel each other under continuous heating, as in the Raman thermometry experiments. By contrast, in the case of pulsed heating, as in the spatiotemporal pump–probe thermometry experiment, the local phonon populations do not necessarily conform to the local strain, whereas phonon refraction due to inhomogeneous dispersion relations is expected to occur at ultrashort timescales, even in the absence of phonon interactions. This results in the following hydro-thermoelastic equation under pulsed heating:

$$\mathbf{q} + \tau \frac{\partial \mathbf{q}}{\partial t} + \kappa \nabla T = \ell^2 \nabla^2 \mathbf{q} + \frac{2kp_t}{bC_v} \nabla \nabla \cdot \mathbf{u}, \quad (2)$$

where \mathbf{u} is the elastic displacement vector, p_t is the phonon pressure, given by $p_t = \frac{T_0 \alpha E}{1-\nu}$, ($T_0 = 300$ K, α is the thermal expansion coefficient,

E is the Young modulus and ν is the Poisson ratio), and b is the averaged phonon group velocity ratio to the phase velocity. This equation, combined with energy conservation and Newton's second law including a linear thermal expansion term (Supplementary Note 1), is a complete mesoscopic model that is capable of predicting heat transport and thermoelastic effects at the nanoscale. In brief, the thermoelastic heat flux term is obtained from the phonon momentum balance in the presence of a time-evolving non-homogeneous strain field. The nanoscale inhomogeneity of the strain profile, originating from thermal expansion, induces a local change in the phonon dispersion relations, which leads to the thermoelastic heat flux contribution included in equation (2) (Supplementary Note 1).

Crucially, we find that only the combination of hydrodynamic and unconventional thermoelastic terms produces a narrow in-phase spatial profile with a sign change as in the experiments (Extended Data Fig. 9c). We validate the theoretical predictions against the experimental data for ultrathin MoSe₂ and MoS₂ samples using *ab initio* results for κ , C_v , τ and b , as well as literature values for the elastic properties³⁰, and limiting the non-local length ℓ to the size of the initial hotspot (Tables 1 and 2). This mesoscopic hydro-thermoelastic model, which is free of fit parameters, predicts the spatial profiles that are in very good agreement with the experimentally observed ones, reproducing the narrow central region, the amplitude of both in-phase and out-of-phase signals,

Table 2 | Hydro-thermoelastic model properties for MoS₂

	Monolayer	Bilayer	Bulk	Reference
ρ (kg m ⁻³)	5,060	5,060	5,060	32
α (K ⁻¹)	5.75×10^{-5}	4.8×10^{-5}	1.15×10^{-5}	30
E (GPa)	250	290	330	35
ν	0.24	0.24	0.24	34
C_v (MJ m ⁻³ K ⁻¹)	1.77	1.77	1.86	Ab initio
κ (W m ⁻¹ K ⁻¹)	53.5	46	43.9	Ab initio
τ (ps)	82.3	82.3	88.4	Ab initio
ℓ (nm)	700	700	70	Supplementary Note 1
b	0.52	0.4863	0.45	Ab initio

For the bilayer system, we use a coefficient of thermal expansion α slightly increased with respect to the literature value.

and the sign change observed in the in-phase component outside the central region (Fig. 3). The regions with negative $\Delta R/R$ become more pronounced when the thickness decreases to the monolayer limit. This is due to the strong variation in the thermoelastic properties, particularly the thermal expansion coefficient (α), with thickness (Tables 1 and 2). For thicker crystals, the thermoelastic effects are weaker, thereby leading to a broader spatial profile, without any sign changes in the in-phase signal.

Comparing diffusive, hydrodynamic and hydro-thermoelastic regimes

To better understand the observations and contributions of each of the diffusive and non-diffusive contributions to heat transport, we analyse the temperature profile at the end of the pump-on window for the three different heat transport regimes: diffusive, hydrodynamic and hydro-thermoelastic regimes. In the purely diffusive case (Fig. 4a), the temperature profile is broad, as expected from classical heat conduction, where thermal gradients drive heat flow evenly from the centre outwards. Next, when we include hydrodynamic effects in the model (Fig. 4b), the temperature profile becomes noticeably narrower. This is because hydrodynamic contributions restrict the heat flow through viscous-like phonon behaviour, effectively impeding the heat propagation. Finally, when we incorporate both hydrodynamic and unconventional thermoelastic effects into the transport equation, the hot region becomes even more localized (Fig. 4c).

The microscopic origin for the very limited heat spreading in the hydro-thermoelastic regime is that thermal expansion in the excitation region induces a strongly inhomogeneous strain and density profile across the sample (Fig. 4d). The thermoelastic contribution to the heat flux, driven by the strain field, points from the compressed (cold) region towards the expanded (hot) region, thereby pointing towards the heated central region of the crystal. Microscopically, this heat flux is a consequence of the different dispersion relations established in compressed and expanded regions, which induces a modification of the momentum accommodated by each phonon mode (Supplementary Note 1). Together with hydrodynamic effects, this produces a very narrow temperature profile that aligns well with the experimental observations for ultrathin flakes.

In conclusion, we have identified strongly impeded heat spreading due to the interplay between hydrodynamic and thermoelastic effects in ultrathin MoSe₂ and MoS₂ crystals at room temperature. The thermoelastic effects are related to the large expansion coefficient of the thinnest crystals, whereas the hydrodynamic effects are caused by the large non-local length ℓ (Supplementary Fig. 1). The latter is probably related to the exceptionally long mean-free path of particularly the flexural modes in the thinnest crystals of these materials^{24,26}. Moreover, our results provide the experimental signatures of two theoretically

predicted, yet experimentally so far not observed, effects, namely, (1) an unconventional thermoelastic heat flux contribution originating from inhomogeneous strain fields at the nanoscale²⁰ and (2) hydrodynamic heat transport in TMDs at room temperature¹⁹. In addition to controllability through thickness and heating type, we predict that the hydro-thermoelastic effects are controllable by the size of the heated region: if this becomes larger than the intrinsic non-local length, for example, hydrodynamic and hydro-thermoelastic effects will not play a role. Our discovery of a novel non-diffusive heat transport regime at room temperature provides important insights into fundamental thermal transport phenomena and has crucial practical implications.

Future research could explore related (two-dimensional) materials, as well as vary the experimental parameters such as temperature and geometry, to further manipulate heat flow. We expect similar hydro-thermoelastic effects to occur in other low-dimensional materials that combine sufficiently large thermal expansion with sufficiently long non-local heat transport lengths. Theoretical work is needed to develop a purely microscopic picture of the impact of the interaction between phonons and elastic fields on thermal transport, which could also be explored using the lattice Boltzmann method³¹. Our discovery of the strong effect of thermoelasticity on pulsed excitation offers possibilities for actively controlling heat flow. The observation that in the hydro-thermoelastic regime heat moves out of a heated region much more slowly than in the case of purely diffusive transport could be interesting for thermoelectric applications. Our studies could lead to tailored thermal management solutions, opening avenues for innovative heat-spreading and heat-routing strategies. Such advancements have the potential to minimize heat loss and improve efficiency in electronic, optoelectronic and photonic devices, thermoelectric systems, and beyond.

Online content

Any methods, additional references, Nature Portfolio reporting summaries, source data, extended data, supplementary information, acknowledgements, peer review information; details of author contributions and competing interests; and statements of data and code availability are available at <https://doi.org/10.1038/s41567-026-03297-1>.

References

1. Fourier, J. B. J. *The Analytical Theory of Heat* (Cambridge Univ. Press, 1878).
2. Casimir, H. B. G. Note on the conduction of heat in crystals. *Physica* **5**, 495–500 (1938).
3. Guyer, R. A. & Krumhansl, J. A. Thermal conductivity, second sound, and phonon hydrodynamic phenomena in nonmetallic crystals. *Phys. Rev.* **148**, 778–788 (1966).
4. Hardy, R. J. Phonon Boltzmann equation and second sound in solids. *Phys. Rev. B* **2**, 1193–1207 (1970).
5. Lane, C. T., Fairbank, H. A. & Fairbank, W. M. Second sound in liquid helium II. *Phys. Rev.* **71**, 600–605 (1947).
6. Narayanamurti, V. & Dynes, R. C. Observation of second sound in bismuth. *Phys. Rev. Lett.* **28**, 1461–1465 (1972).
7. Jackson, H. E., Walker, C. T. & McNelly, T. F. Second sound in NaF. *Phys. Rev. Lett.* **25**, 26–28 (1970).
8. Koreeda, A., Takano, R. & Saikan, S. Second sound in SrTiO₃. *Phys. Rev. Lett.* **99**, 265502 (2007).
9. Huberman, S. et al. Observation of second sound in graphite at temperatures above 100 K. *Science* **364**, 375–379 (2019).
10. Beardo, A. et al. Observation of second sound in a rapidly varying temperature field in Ge. *Sci. Adv.* **7**, eabg4677 (2021).
11. Machida, Y. et al. Observation of Poiseuille flow of phonons in black phosphorus. *Sci. Adv.* **4**, eaat3374 (2018).
12. Smontara, A., Lasjaunias, J. C. & Maynard, R. Phonon Poiseuille flow in quasi-one-dimensional single crystals. *Phys. Rev. Lett.* **77**, 5397 (1996).

13. Martelli, V., Jiménez, J. L., Continentino, M., Baggio-Saitovitch, E. & Behnia, K. Thermal transport and phonon hydrodynamics in strontium titanate. *Phys. Rev. Lett.* **120**, 125901 (2018).
14. Huang, X. et al. Observation of phonon Poiseuille flow in isotopically purified graphite ribbons. *Nat. Commun.* **14**, 2044 (2023).
15. Machida, Y., Matsumoto, N., Isono, T. & Behnia, K. Phonon hydrodynamics and ultrahigh-room-temperature thermal conductivity in thin graphite. *Science* **367**, 309–312 (2020).
16. Ziabari, A. et al. Full-field thermal imaging of quasiballistic crosstalk reduction in nanoscale devices. *Nat. Commun.* **9**, 255 (2018).
17. Xiang, Z., Jiang, P. & Yang, R. Time-domain thermoreflectance (TDTR) data analysis using phonon hydrodynamic model. *J. Appl. Phys.* **132**, 205104 (2022).
18. Beardo, A. et al. A general and predictive understanding of thermal transport from 1D- and 2D-confined nanostructures: theory and experiment. *ACS Nano* **15**, 13019–13030 (2021).
19. Cepellotti, A. et al. Phonon hydrodynamics in two-dimensional materials. *Nat. Commun.* **6**, 6400 (2015).
20. Kronig, R. On the hydrodynamics of non-viscous fluids and the theory of helium II. Part III. *Physica* **19**, 535–544 (1953).
21. Varghese, S. et al. A pre-time-zero spatiotemporal microscopy technique for the ultrasensitive determination of the thermal diffusivity of thin films. *Rev. Sci. Instrum.* **94**, 034903 (2023).
22. Kim, S. et al. Extremely anisotropic van der Waals thermal conductors. *Nature* **597**, 660–665 (2021).
23. Xiao, P. et al. MoS₂ phononic crystals for advanced thermal management. *Sci. Adv.* **10**, eadm8825 (2024).
24. Reig, D. S. et al. Unraveling heat transport and dissipation in suspended MoSe₂ from bulk to monolayer. *Adv. Mater.* **34**, 2108352 (2022).
25. Jiang, P., Qian, X., Gu, X. & Yang, R. Probing anisotropic thermal conductivity of transition metal dichalcogenides MX₂ (M = Mo, W and X = S, Se) using time-domain thermoreflectance. *Adv. Mater.* **29**, 1701068 (2017).
26. Farris, R. et al. Microscopic understanding of the in-plane thermal transport properties of 2H transition metal dichalcogenides. *Phys. Rev. B* **109**, 125422 (2024).
27. Guyer, R. A. & Krumhansl, J. A. Solution of the linearized phonon Boltzmann equation. *Phys. Rev.* **148**, 766–778 (1966).
28. Sendra, L. et al. Derivation of a hydrodynamic heat equation from the phonon Boltzmann equation for general semiconductors. *Phys. Rev. B* **103**, L140301 (2021).
29. Beardo, A. et al. Hydrodynamic heat transport in compact and holey silicon thin films. *Phys. Rev. Appl.* **11**, 034003 (2019).
30. Hu, X. et al. Mapping thermal expansion coefficients in freestanding 2D materials at the nanometer scale. *Phys. Rev. Lett.* **120**, 055902 (2018).
31. D’Orazio, A., Succi, S. & Arrighetti, C. Lattice Boltzmann simulation of open flows with heat transfer. *Phys. Fluids*. **15**, 2778–2781 (2003).
32. Rumble, J. R. *CRC Handbook of Chemistry and Physics* (CRC Press, 2018).
33. Babacic, V. et al. Thickness-dependent elastic softening of few-layer free-standing MoSe₂. *Adv. Mater.* **33**, 2008614 (2021).
34. Zeng, F., Zhang, W.-B. & Tang, B.-Y. Electronic structures and elastic properties of monolayer and bilayer transition metal dichalcogenides MX₂ (M = Mo, W; X = O, S, Se, Te): a comparative first-principles study. *Chin. Phys. B* **24**, 097103 (2015).
35. Liu, K. & Wu, J. Mechanical properties of two-dimensional materials and heterostructures. *J. Mater. Res.* **31**, 832–844 (2016).

Publisher’s note Springer Nature remains neutral with regard to jurisdictional claims in published maps and institutional affiliations.

Open Access This article is licensed under a Creative Commons Attribution-NonCommercial-NoDerivatives 4.0 International License, which permits any non-commercial use, sharing, distribution and reproduction in any medium or format, as long as you give appropriate credit to the original author(s) and the source, provide a link to the Creative Commons licence, and indicate if you modified the licensed material. You do not have permission under this licence to share adapted material derived from this article or parts of it. The images or other third party material in this article are included in the article’s Creative Commons licence, unless indicated otherwise in a credit line to the material. If material is not included in the article’s Creative Commons licence and your intended use is not permitted by statutory regulation or exceeds the permitted use, you will need to obtain permission directly from the copyright holder. To view a copy of this licence, visit <http://creativecommons.org/licenses/by-nc-nd/4.0/>.

© The Author(s) 2026

Methods

Experimental details

MoSe₂ and MoS₂ flakes of varying thicknesses were mechanically exfoliated from bulk crystals onto a viscoelastic polydimethylsiloxane stamp and subsequently transferred using a dry-transfer technique onto titanium (5 nm)/gold (50 nm)-coated silicon nitride substrates containing circular holes with a diameter of 15 μm (Norcada, NTPR005D-C15), resulting in suspended flakes. The flakes are monocrystalline and exhibit clean surfaces and low strain³⁶. For the measurements, we used samples suspended over the 15-μm holes, with similar results also obtained for the 10-μm holes (Supplementary Fig. 2). The spatiotemporal pump–probe thermometry setup (Extended Data Fig. 2 and ref. 21) uses a FLINT laser from LIGHT CONVERSION, operating at a frequency of 76 MHz, which produces pulses centred at 1,030 nm with <200-fs temporal resolution. The majority of the laser power drives an optical parametric oscillator that generates a variable signal output ranging from 1,320 to 2,000 nm. We use the second or third harmonic of this signal output as probe, tuning it to the exciton resonances—800 nm for MoSe₂ and 615 nm for MoS₂. Utilizing a scanning mirror system (Optics in Motion OIM101), we control the probe's direction, whereas the pump beam (at 515 nm, the second harmonic of the fundamental laser source) goes through a Newport DL255 delay line and an electro-optic modulator that controls the pump modulation frequency f_{mod} (240 kHz). Both beams are combined using a dichroic mirror and then focused to submicrometre spots via a microscope objective lens with a numerical aperture of 0.65. The pump and probe spot sizes are $\sigma_{\text{pu}} \approx 0.27$ μm and $\sigma_{\text{pr}} \approx 0.35$ μm, respectively. We detect the reflected probe beam using a silicon photodiode.

The spatiotemporal pump–probe thermometry measurements, described in detail in ref. 21, rely on the fact that within a nanosecond³⁷, energy from the initial pump-induced electronic excitation transfers to the lattice, where phonons transport the energy as lattice heat towards the metallic heat sink at the edge of the suspended crystal, which takes place on a microsecond timescale (Extended Data Fig. 3). In the case of purely diffusive heat transport following Fourier's law, this leads to a spatial temperature profile that exclusively depends on thermal diffusivity, the accurately known geometry of the system, and two frequencies related to the pulsed photoexcitation: the laser repetition rate f_{rep} and the pump modulation frequency f_{mod} . Measuring the spatial profile, thus, provides direct access to thermal diffusivity. We record the spatial profile at a slightly negative pump–probe delay, corresponding to a delay time of $1/f_{\text{rep}} \approx 13$ ns, where the transient reflectivity results from the pump-induced lattice temperature change, without any contribution from the photoexcited electronic species. The transient reflectivity is sensitive to the lattice temperature ΔT via the temperature-dependent exciton linewidth³⁸. We modulate the intensity of the pump beam at a frequency $f_{\text{mod}} = 240$ kHz and demodulate using a lock-in amplifier (Zurich MFLI), obtaining in-phase and out-of-phase signals. We perform all measurements in a vacuum ($\sim 10^{-5}$ mbar) and at room temperature.

To ensure that we can accurately correlate the transient reflectivity signal to a lattice temperature, we need to operate in the linear regime, where an increase in pump fluence gives a proportional increase in temperature and, therefore, transient reflectivity. To confirm that we are in the linear regime in our experiments, we first conduct temporal dynamics measurements by varying the pump fluence. In addition, we perform spatial scans on the suspended region by varying the pump fluence. Extended Data Fig. 6a–d shows the results obtained for an almost eight-layer MoSe₂ sample. Both in-phase and out-of-phase signals exhibit a linear increase with pump fluence, as evident from their respective normalized plots. This linear dependence of the signal supports the use of the transient reflectivity profile as a representation of the spatial temperature profile. Moreover, we vary the probe fluence (and fix the pump power) on the suspended trilayer MoSe₂ sample, yielding similar observations (Extended Data Fig. 6e–h). On the basis

of these measurements, we keep the pump and probe fluences in the range of 6–20 μJ cm⁻², to ensure that the system is in a regime in which the transient reflectivity scales linearly with pump power (Extended Data Figs. 5, 6 and 10). In this case, the typical temperature increase is on the order of 10 K.

Given recent reports that layered semiconductors can exhibit exotic electron–hole plasma³⁹ phases due to strong electron interactions, we conducted photoluminescence (PL) measurements on a monolayer MoSe₂ sample to confirm that we are operating within the linear electronic regime. This ensures that our observations are not influenced by nonlinear electron–hole plasma effects. Extended Data Fig. 10a displays the PL spectra with increasing laser fluence (pump, 515 nm). Consistently, we observe a linear increase in spectral average (area under PL spectrum) with laser fluence (Extended Data Fig. 10b), suggesting that we are well below the Mott transition limit and ruling out the presence of such exotic phases. In particular, we conduct these PL measurements under almost identical configurations as the spatiotemporal thermometry measurements, with the only difference being the collection of PL emission by a fibre cable to the spectrometer (Extended Data Fig. 10c).

Phenomenological diffusive Fourier model

To obtain an effective diffusivity from the transient reflectivity evolution observed in our experiments, we use Fourier's diffusive heat law to model the propagation of heat from the localized pump-induced hotspot to the heat sink:

$$\frac{\partial T}{\partial t} = D\nabla^2 T + \frac{Q}{C_v}, \quad (3)$$

where T is the lattice temperature, t is time, D is the diffusivity, Q is the power injected by the pump laser and C_v is the heat capacity. Initially, we start with a Gaussian temperature profile that represents the localized heating from a single pump pulse. As time progresses, this temperature profile diffuses outwards and decays, as heat flows towards the heat sink. Due to the relatively short time interval between consecutive laser pulses (13 ns, corresponding to the 76-MHz repetition rate, f_{rep}), the temperature profile does not fully return to equilibrium before the next pump pulse arrives.

At $t = 13$ ns (or $t = \frac{1}{f_{\text{rep}}}$), we inject a Gaussian energy pulse into the existing, partially decayed, temperature distribution. This cycle repeats until the end of the pump-on window. The number of these Gaussian pulses (N) that contribute to the accumulated heat during the pump-on window is determined by the laser repetition rate and the pump modulation frequency (f_{mod}), given by $N = \frac{f_{\text{rep}}}{2f_{\text{mod}}}$ for a 50% duty cycle (160 pulses in our case). When the pump is blocked during the pump-off window, the accumulated heat fully dissipates. The heating cycle then resumes with the next pump-on window.

We perform our simulations in two dimensions with radial symmetry and calculate the temperature rise $\Delta T(x, y)$ over time using the forward-time centred-space finite difference method. We set the boundary condition at $r = 7.5$ μm (the edge of the suspended region) as a perfect heat sink, $\Delta T = 0$ K, to represent the gold-coated substrate. To obtain the in-phase and out-of-phase convoluted transient reflectivity profiles from the model predictions, we perform the lock-in operations described in the 'Describing in-phase and out-of-phase signals' section.

DFT input for the mesoscopic model

The ab initio calculations are conducted using density functional theory as implemented in the SIESTA program^{40,41}, as described in detail in ref. 26. Briefly, the cell and atomic positions are optimized using a conjugate gradient method, ensuring that the maximum forces on atoms are kept below 10^{-5} eV Å⁻¹. For low-dimensional structures, a vacuum thickness of 17 Å is used to avoid periodic interactions along the stacking direction. Unlike in ref. 24, we do not normalize the

thermal conductivity taking into account this additional volume. All calculations use the Perdew–Burke–Ernzerhof generalized gradient approximation^{42,43} with van der Waals functionals, as reparameterized in ref. 44. A k -mesh of $20 \times 20 \times 1$ is used for monolayers, bilayers and trilayers, and $20 \times 20 \times 20$ for other systems, with norm-conserving pseudopotentials⁴⁵ sourced from the PseudoDojo library⁴⁶.

To compute the interatomic force constants (IFCs), we generate supercells of size $10 \times 10 \times 10$ for bulk systems and $10 \times 10 \times 1$ for the other structures. Atomic displacements are thermally initialized using a Bose–Einstein distribution, simulating phonons at 300 K, using TDEP routines⁴⁷. With these thermally populated supercells, we calculate both second- and third-order IFCs, with real-space force cut-offs of 5 Å for the third-order IFCs and 8 Å for the second-order IFCs. Thermal properties calculations are subsequently conducted on a q -point grid of $128 \times 128 \times 1$ for monolayers, $64 \times 64 \times 1$ for bilayers and trilayers, and $24 \times 24 \times 24$ for bulk systems. The thermal properties calculated for MoSe₂ and MoS₂ are presented in Tables 1 and 2, respectively, and serve as input parameters for our mesoscopic model. Specifically, we directly obtain the heat capacity C_v , and use the full solution of the Boltzmann transport equation to obtain the thermal conductivity κ . Furthermore, the mode-resolved lifetimes τ_λ , group velocities v_λ and phase velocities c_λ serve as input parameters to obtain the heat flux relaxation time τ and the non-local length ℓ used in the hydrodynamic transport equation that we describe later²⁸.

Hydro-thermoelastic model

The hydrodynamic and thermoelastic model predictions of the convoluted thermal profiles are obtained by solving the hydro-thermoelastic transport equation (equation (2)), along with the energy balance equation including thermomechanical energy exchange, and Newton's law for the elastic field evolution including a linear thermal expansion term (Supplementary Note 1). Numerical solutions are obtained using finite elements²⁹. In Tables 1 and 2, we present the intrinsic thermoelastic parameter values appearing in the model equations for MoSe₂ and MoS₂, respectively. In the absence of hydrodynamic and thermoelastic effects, the hydro-thermoelastic equation reduces to Fourier's law. By combining this simplified transport equation with the energy balance equation, one recovers the thermal diffusion equation described in the 'Phenomenological diffusive Fourier model' section.

We impose radial symmetry and restrict the deformation to the in-plane directions. The temperature and displacement in the edges of the sample are fixed. The excitation is modelled as a Gaussian power density in the energy balance equation with a characteristic size of $L = 700$ nm, which is assumed to be larger than the optical spot size to account for fast diffusion of the optically excited hot electrons and excitons before they deposit energy into the lattice⁴⁸. We note that the resulting temperature profiles are qualitatively insensitive to the exact size of the thermal source. In the time domain, the excitation power density follows a square function with a frequency of 240 kHz. Thus, we do not explicitly simulate the energy pulses during the pump-on stage, as described earlier. This simplification greatly reduces the computational cost by preventing the propagation of acoustic waves, and we verified that it does not significantly modify the average temperature and elastic fields predicted by the model (Supplementary Fig. 3). Finally, to obtain the in-phase and out-of-phase convoluted thermal profiles from the model predictions, we perform the lock-in operations described in the 'Describing in-phase and out-of-phase signals' section. More details are provided in Supplementary Note 1.

Describing in-phase and out-of-phase signals

To model the photoresponse, specifically the in-phase and out-of-phase signals, we use the results of the simulations from both the phenomenological diffusive Fourier model and the mesoscopic hydrodynamic and thermoelastic models, and simulate the lock-in detection process. As an example, Extended Data Fig. 4a shows the temperature dynamics

obtained from the Fourier model over multiple modulation cycles. First, we examine the case with a thermal diffusivity of $0.20 \text{ cm}^2 \text{ s}^{-1}$ at a modulation frequency f_{mod} of 10 kHz. The temperature rises during the pump-on period, reaching its peak by the end of this window, and then decays during the pump-off period, returning to zero in approximately 2 μs during the pump-off window (Extended Data Fig. 4a).

To simulate the lock-in operation, we multiply this temperature signal by a sine function (to obtain the in-phase signal) and a cosine function (to obtain the out-of-phase signal), both at the modulation frequency of the pump (Extended Data Fig. 4b,c). We obtain the in-phase and out-of-phase signals by averaging these products over time. Repeating this process for temperature dynamics at different spatial positions (from the hotspot to the heat sink) allows us to reconstruct the in-phase and out-of-phase spatial profiles (Extended Data Fig. 4d). The cosine-weighted temperature dynamics average out to nearly zero, whereas the sine-weighted dynamics remain finite, indicating a predominantly in-phase response and a negligible out-of-phase contribution.

Next, we consider a higher modulation frequency, $f_{\text{mod}} = 240$ kHz, and repeat the Fourier simulation with $D = 0.20 \text{ cm}^2 \text{ s}^{-1}$. Extended Data Fig. 4e shows the resulting temperature dynamics at various spatial positions. The temperature rises during the pump-on period, reaches its maximum near the end of this window, and then decays during the pump-off period, returning nearly to zero before the onset of the next pump-on cycle. Unlike the 10-kHz case, a finite-temperature signal persists during the pump-off window. This key difference leads to a finite out-of-phase contribution when averaging the cosine-weighted temperature dynamics (Extended Data Fig. 4f–h).

Finally, we consider the case of a lower diffusivity, $0.02 \text{ cm}^2 \text{ s}^{-1}$, and repeat the Fourier simulation at $f_{\text{mod}} = 240$ kHz. Extended Data Fig. 4i illustrates the temperature dynamics for this scenario at various spatial positions. Two key differences emerge. First, as shown in Extended Data Fig. 3, the temperature does not fully decay during the pump-off period, unlike in the case of higher diffusivity. Second, around 2 μm from the heat source, the temperature rises slowly during the pump-on window and decays equally slowly during the pump-off window. The lower diffusivity causes heat to propagate more slowly, resulting in delayed temperature rise, with the maximum temperature at 2 μm occurring during the pump-off phase.

This delayed heating causes the temperature dynamics at this location to be π out of phase, leading to a sign change in the in-phase signal. Note that the out-of-phase signal is $\pi/2$ out of phase with respect to the in-phase signal. Mathematically, these negative in-phase signals occur because when the temperature dynamics are multiplied by the sine wave, a substantial portion of the sine's negative part overlaps with the temperature during the pump-off period. Consequently, after averaging, certain regions in the in-phase spatial profile exhibit sign changes (Extended Data Fig. 4j–l). In summary, the observed sign change in the in-phase signal in our experiments does not indicate negative differential temperatures but is a result of the lock-in operation. This phenomenon becomes apparent when there is a slow, highly viscous flow of heat, as seen in ultrathin layered semiconductors (see the main text) with low thermal diffusivity.

DFT details for LBTE calculations

As an independent approach, we perform LBTE calculations that include non-diffusive effects, except for thermoelastic effects. We follow the strategy presented in ref. 49 to solve the LBTE:

$$\frac{\partial g_n}{\partial t} + \mathbf{v}_n \cdot \nabla g_n = Qp_n + \sum_j \omega_n W_{nj} \frac{1}{\omega_j} (c_j \Delta T - g_j), \quad (4)$$

where g_n is the deviational phonon energy density per mode, Q is the macroscopic volumetric heat generation rate and the values p_n describe the distribution of heating among the phonon modes. The continuous

integral of the collision term in the Boltzmann transport equation has been discretized as matrix $W_{n,j}$, which is a general scattering matrix of dimensions $M \times M$ describing the scattering rate between phonon states n and j , acting on the difference between the equilibrium and non-equilibrium distribution functions. The heat generation rate expressed as $Q = \delta(t)\chi(x)$, where $\delta(t)$ is the Dirac delta, corresponds to impulse laser heating with a spatial intensity profile $\chi(x)$. The temperature T is defined⁴⁹ as the value for which the equilibrium energy density of phonons matches the non-equilibrium energy density. Linearization gives the temperature rise ΔT as the ratio of the non-equilibrium energy density of phonons divided by the heat capacity C_v :

$$\Delta T = \frac{1}{C_v} \sum_n g_n. \quad (5)$$

To obtain the necessary inputs for the LBTE and ballistic predictions, we performed DFT calculations using the QUANTUM ESPRESSO package. Several pseudopotentials and exchange–correlation functionals were tested including the full relativistic norm-conserving pseudopotential, ultrasoft pseudopotentials and standard solid-state pseudopotentials with the Perdew–Burke–Ernzerhof generalized gradient approximation and PBEsol. The DFT calculation parameters used in this work are as follows: a $20 \times 20 \times 1$, $20 \times 20 \times 1$, $16 \times 16 \times 16$ and $16 \times 16 \times 16$ Monkhorst–Pack k -mesh with a kinetic energy cut-off of 110, 120, 100 and 100 Ry and convergence criteria of 1×10^{-15} , 1×10^{-16} , 1×10^{-14} , 1×10^{-14} Ry is used for monolayer MoS₂, monolayer MoSe₂, bulk MoS₂ and bulk MoSe₂, respectively. $8 \times 8 \times 1$, $8 \times 8 \times 1$, $4 \times 4 \times 4$ and $4 \times 4 \times 4$ second-order force constant supercells and $4 \times 4 \times 1$, $4 \times 4 \times 1$, $4 \times 4 \times 4$ and $4 \times 4 \times 4$ third-order force constants up to the fifth nearest neighbour were used, where only wavefunctions at the gamma point were considered for extraction of the third-order force constants for monolayer MoS₂, monolayer MoSe₂, bulk MoS₂ and bulk MoSe₂, respectively. DFT and Boltzmann transport equation input and output files are available via GitHub at <https://github.com/jamalabouhaibeh/Calculations>. The results for the ballistic regime are described in Supplementary Note 2 and Supplementary Figs. 4 and 5.

Data availability

The data supporting the findings of this study are provided in the article and its Supplementary Information. Source data are provided with this paper. Source data are also available via Zenodo at <https://doi.org/10.5281/zenodo.19114529> (ref. 50).

References

- Varghese, S. et al. Fabrication and characterization of large-area suspended MoSe₂ crystals down to the monolayer. *J. Phys. Mat.* **4**, 046001 (2021).
- Kumar, N. et al. Exciton diffusion in monolayer and bulk MoSe₂. *Nanoscale* **6**, 4915–4919 (2014).
- Selig, M. et al. Excitonic linewidth and coherence lifetime in monolayer transition metal dichalcogenides. *Nat. Commun.* **7**, 13279 (2016).
- Bataller, A. W. et al. Dense electron–hole plasma formation and ultralong charge lifetime in monolayer MoS₂ via material tuning. *Nano Lett.* **19**, 1104–1111 (2019).
- Soler, J. M. et al. The SIESTA method for ab initio order- N materials simulation. *J. Phys.: Condens. Matter* **14**, 2745 (2002).
- García, A. et al. SIESTA: recent developments and applications. *J. Chem. Phys.* **152**, 204108 (2020).
- Perdew, J. P., Burke, K. & Ernzerhof, M. Generalized gradient approximation made simple. *Phys. Rev. Lett.* **77**, 3865 (1996).
- Perdew, J. P., Burke, K. & Ernzerhof, M. Generalized gradient approximation made simple. *Phys. Rev. Lett.* **78**, 1396 (1997).
- Lee, K., Murray, É. D., Kong, L., Lundqvist, B. I. & Langreth, D. C. Higher-accuracy van der Waals density functional. *Phys. Rev. B* **82**, 081101 (2010).

- García, A., Verstraete, M. J., Pouillon, Y. & Junquera, J. The PSML format and library for norm-conserving pseudopotential data curation and interoperability. *Comput. Phys. Commun.* **227**, 51–71 (2018).
- van Setten, M. et al. The PseudoDojo: training and grading a 85 element optimized norm-conserving pseudopotential table. *Comput. Phys. Commun.* **226**, 39–54 (2018).
- Knoop, F. et al. TDEP: temperature dependent effective potentials. *J. Open Source Softw.* **9**, 6150 (2024).
- Lo Gerfo Morganti, G. et al. Transient ultrafast and negative diffusion of charge carriers in suspended MoSe₂ from multilayer to monolayer. *Nat. Commun.* **16**, 5184 (2025).
- Chiloyan, V. et al. Green's functions of the Boltzmann transport equation with the full scattering matrix for phonon nanoscale transport beyond the relaxation-time approximation. *Phys. Rev. B* **104**, 245424 (2021).
- Varghese, S. et al. Source data for: Controllable hydro-thermoelastic heat transport in ultrathin semiconductors at room temperature. *Zenodo* <https://doi.org/10.5281/zenodo.19114528> (2026).

Acknowledgements

We thank M. Verstraete for useful discussions. ICN2 is funded by the CERCA Programme/Generalitat de Catalunya and supported by the Severo Ochoa Centres of Excellence programme, Grant CEX2021-001214-S, funded by MCIN/AEI/10.13039/501100011033. K.J.T. acknowledges funding from the European Union's Horizon 2020 research and innovation programme under grant agreement number 804349 (ERC StG 'CUHL') and Spanish MCIN/AEI project PID2022-142730NB-I00 ('HYDROPTO'). S.H. acknowledges funding from the NSERC Discovery Grant program (RGPIN-2021-02957) and the FRQNT Nouveau Chercheur program (341503) and computational resources provided by Calcul Québec, Compute Ontario and the Digital Research Alliance of Canada. J.T.-P., J.C., A.B. and F.X.A. acknowledge financial support from the Spanish Ministerio de Ciencia, Innovación y Universidades under grant number PID2021-122322NB-I00 and TED2021-129612B-C22 (MCIU/AEI/10.13039/501100011033/FEDER UE) and the AGAUR—Generalitat de Catalunya under grant number 2021-SGR-00644. R.F. and P.O. acknowledge financial support from EU 'MaX' CoE (grant number 101093374), grant numbers PID2022-139776NB-C62 and PCI2022-134972-2 funded by Spanish MCIN/AEI/10.13039/501100011033 and by ERDF, A way of making Europe, and grant number 2021SGR1519 from AGAUR—Generalitat de Catalunya.

Author contributions

K.J.T. conceived of and directed the work and supervised the experimental part. F.X.A. supervised the main theoretical part. S.V. and D.S.R. prepared the samples. S.V. performed the measurements with input from J.D.M. and K.J.T. S.V. analysed the experimental results and performed the simulations of the experiment using Fourier's model, with input from K.J.T. A.B., J.C., J.T.-P. and F.X.A. developed and implemented the mesoscopic model. R.F. performed the ab initio calculations that served as input for the mesoscopic model, with input from P.O. S.H., A.S. and J.A.H. performed the LBTE simulations. A.B., K.J.T., F.X.A., S.H., S.V. and J.T.-P. discussed and interpreted the experimental and theoretical results. S.V., A.B., S.H. and K.J.T. drafted the paper, with input from all authors.

Competing interests

The authors declare no competing interests.

Additional information

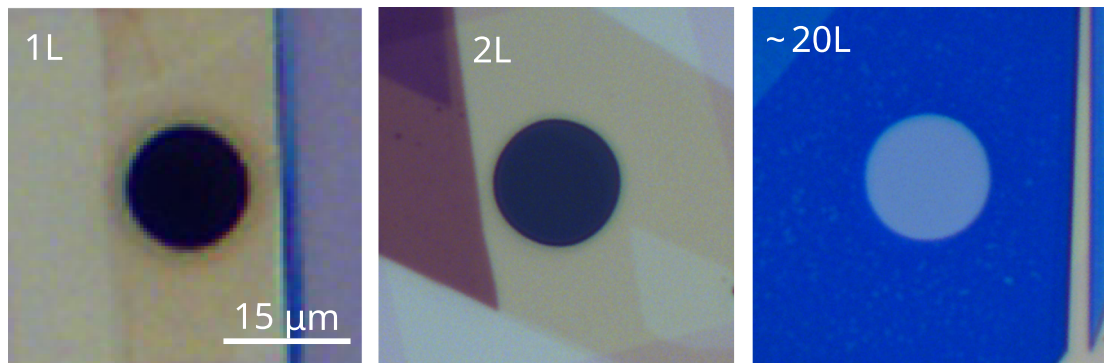
Extended data is available for this paper at <https://doi.org/10.1038/s41567-026-03297-1>.

Supplementary information The online version contains supplementary material available at <https://doi.org/10.1038/s41567-026-03297-1>.

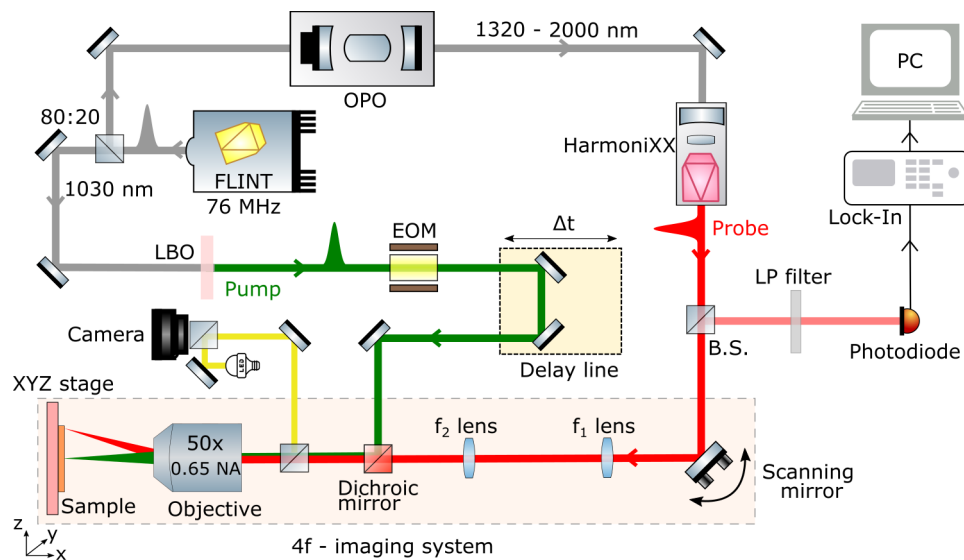
Correspondence and requests for materials should be addressed to K. J. Tielrooij.

Peer review information *Nature Physics* thanks Peijun Guo, Sauro Succi and the other, anonymous, reviewer(s) for their contribution to the peer review of this work.

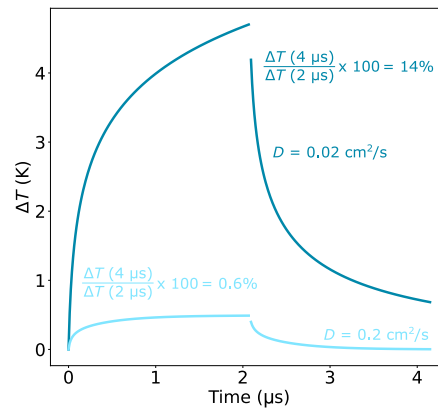
Reprints and permissions information is available at www.nature.com/reprints.



Extended Data Fig. 1 | Suspended MoS₂ samples. Optical microscope images of the measured suspended MoS₂ samples. The scale bar (15 μm) for monolayer (1L) is valid for all the images. For details on sample fabrication and characterization, see ref. 36.

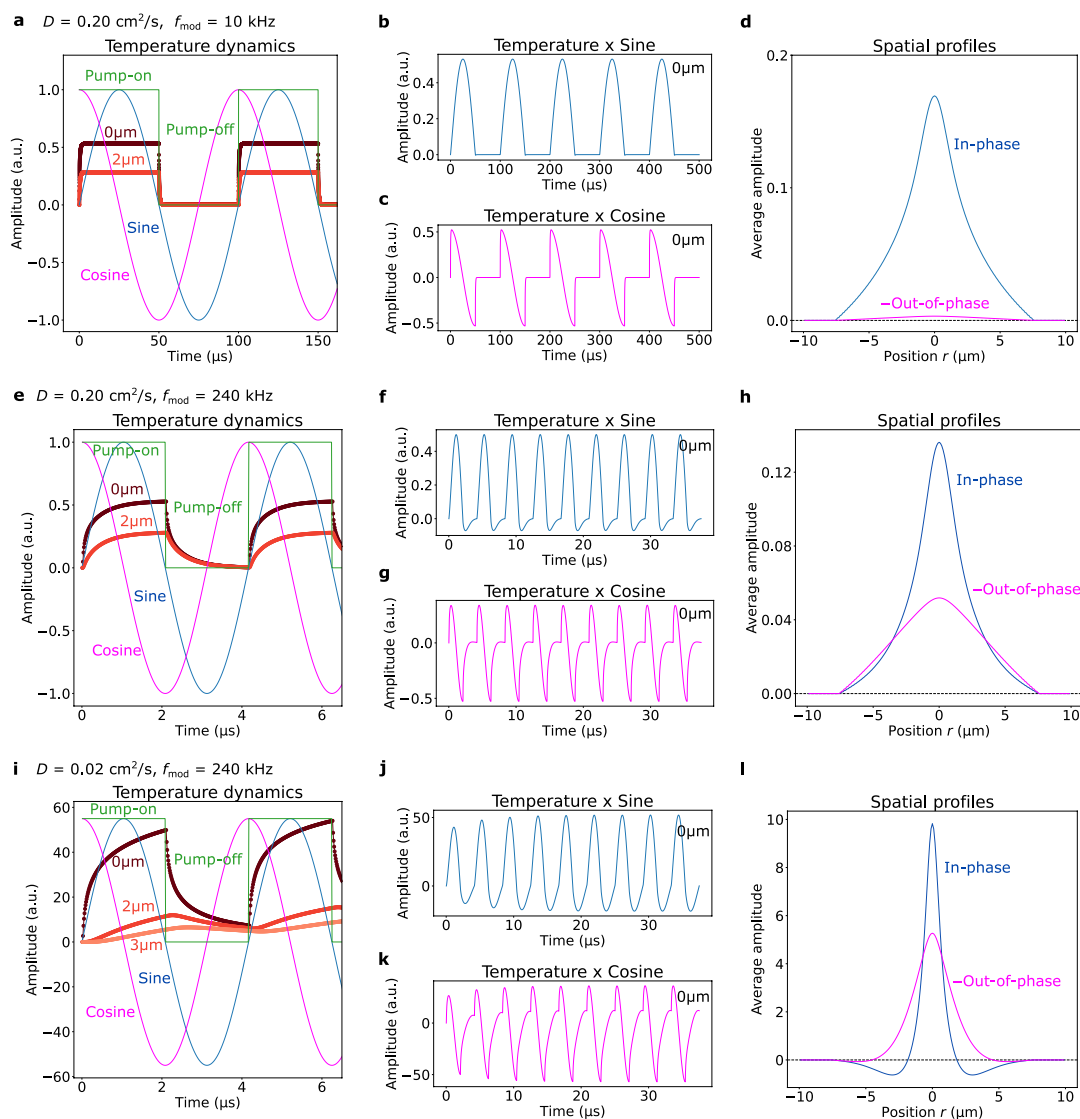


Extended Data Fig. 2 | Detailed schematic of the spatiotemporal thermometry setup. OPO: Optical Parametric Oscillator, EOM: Electro-Optic Modulator, LBO: lithium triborate crystal, LP: longpass filter, B.S.: beam splitter. For more details, see ref. 21.

**Extended Data Fig. 3 | Temperature decay due to in-plane heat diffusion.**

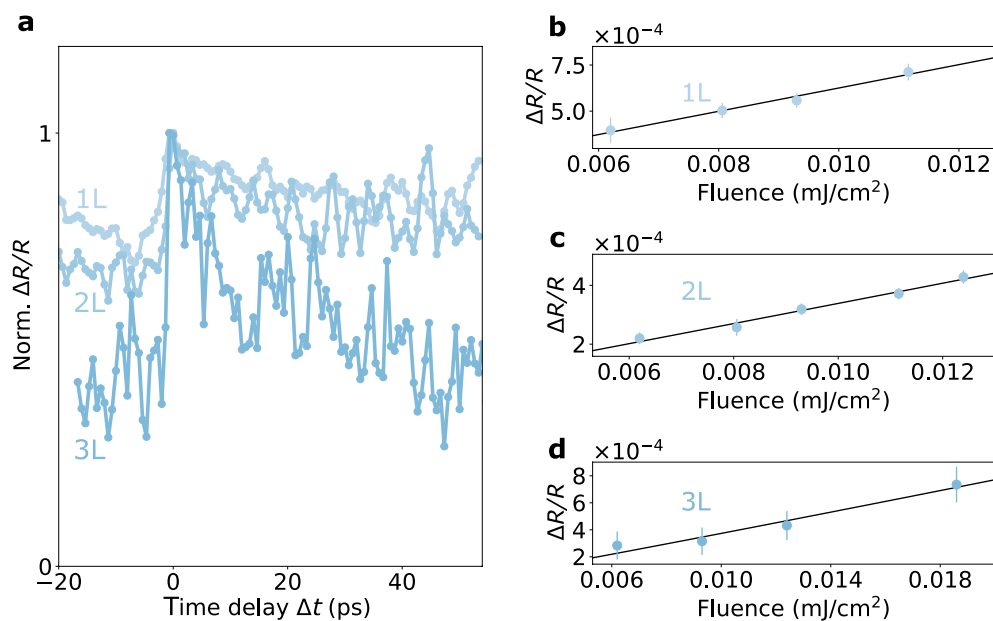
Temperature dynamics as calculated using the phenomenological Fourier model over a full modulation window of $4 \mu\text{s}$ (1/240 kHz). A relatively large thermal diffusivity of $0.20 \text{ cm}^2/\text{s}$ leads to efficient heat spreading to the heat sink at the edges of the suspended crystal. Consequently, less heat accumulates within each

cycle, enabling the system to reach thermal equilibrium before the subsequent pump-on window. In contrast, a lower thermal diffusivity of $0.02 \text{ cm}^2/\text{s}$ leads to slower heat spreading, resulting in more heat accumulation, and leftover heat at the end of the modulation period.



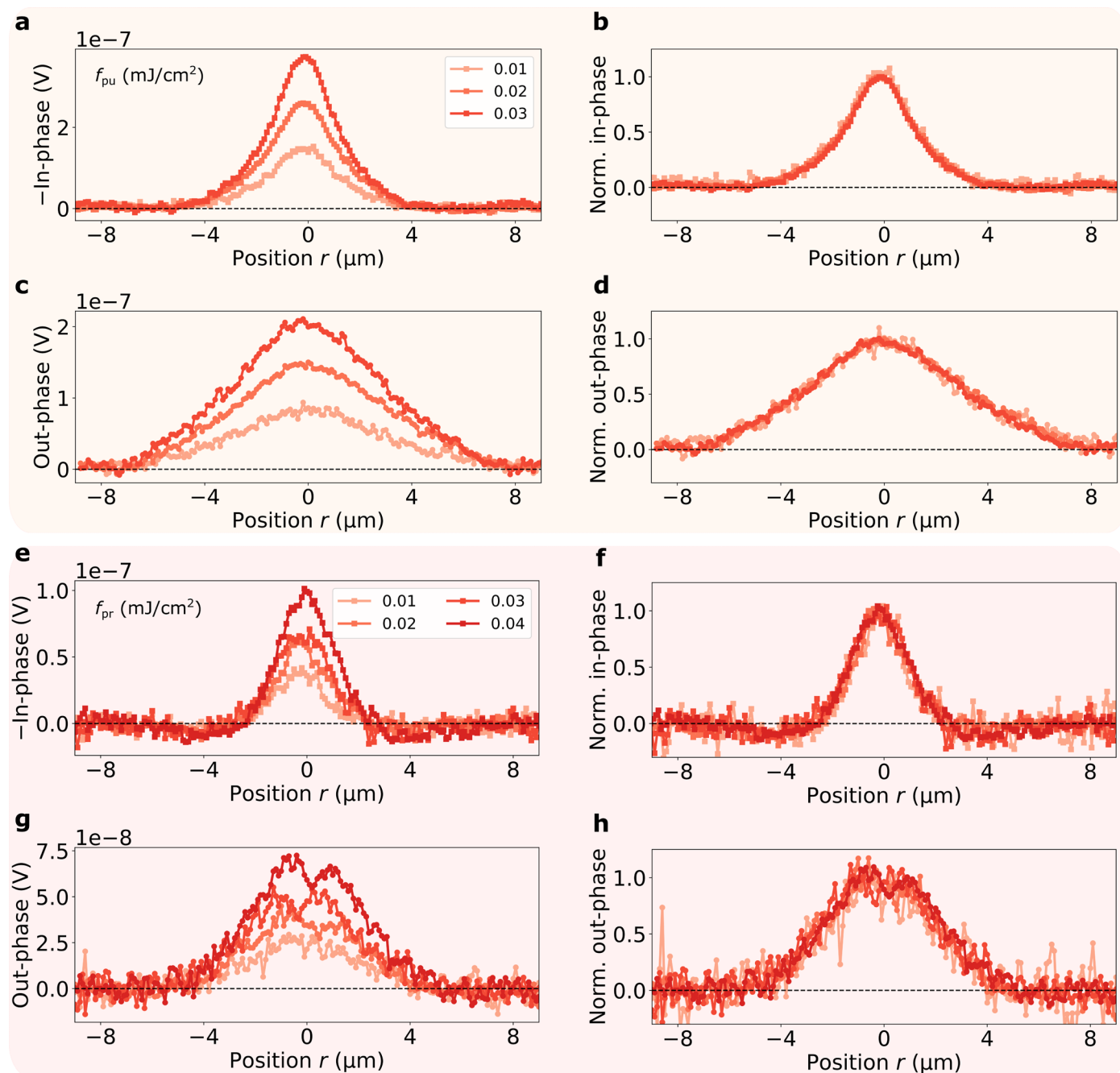
Extended Data Fig. 4 | The lock-in operation demonstrated with the phenomenological Fourier model. **a**, Temperature dynamics obtained from the diffusive Fourier model using a diffusivity of $D = 0.20 \text{ cm}^2/\text{s}$ at two different locations, namely $r = 0$ and $2 \mu\text{m}$ from the central hotspot, during square wave modulation ($f_{\text{mod}} = 10 \text{ kHz}$) cycles. **b**, **c**, Temperature dynamics multiplied by sine (b) and cosine (c) functions. **d**, Resulting in-phase and out-of-phase spatial profiles after averaging the sine- and cosine-multiplied temperature dynamics at

different spatial positions r . **e–l**, The same results ($f_{\text{mod}} = 240 \text{ kHz}$) using a diffusivity of $D = 0.20 \text{ cm}^2/\text{s}$ (e–h) and $D = 0.02 \text{ cm}^2/\text{s}$ (i–l). **l**, The in-phase and out-of-phase spatial profiles obtained for $D = 0.02 \text{ cm}^2/\text{s}$, where in-phase profiles show a dip with negative signal a few micrometers away from the central hotspot. The out-of-phase profiles in panels **d**, **h**, and **l** are multiplied by -1 for convenient comparison.



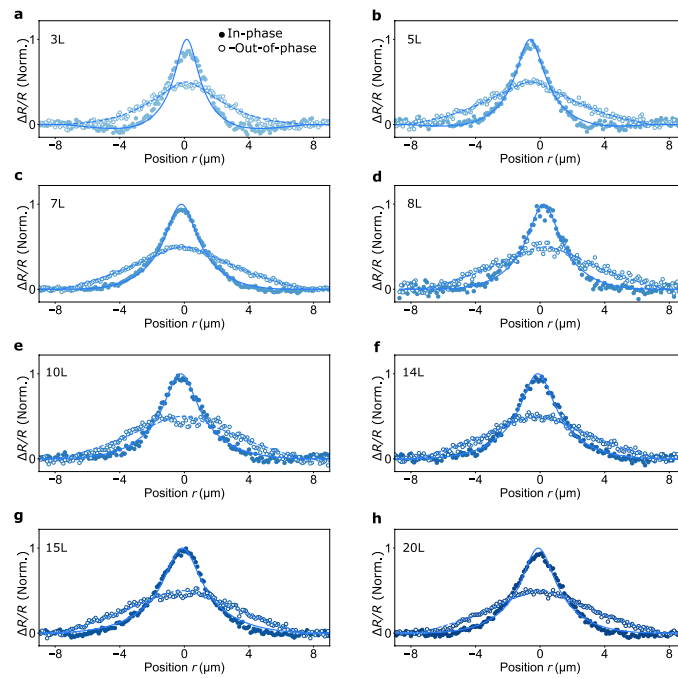
Extended Data Fig. 5 | Decay dynamics and pump fluence dependence on $\Delta R/R$. **a**, Temporal dynamics on the suspended region of mono-, bi-, and trilayer MoSe_2 flake. As discussed in the main text and in detail in Ref. 21, the signal at $\Delta t < 0$ (or $\Delta t = 13$ ns) represents the phonon heat accumulated in the system. Thinner flakes show more heat accumulation due to less efficient heat transport

to the heat sinks. **b–d**, The transient reflectivity signals at $\Delta t = 13$ ns show a linear dependence with pump fluence for monolayer (b), bilayer (c), and trilayer (d) MoSe_2 samples, which makes the transient reflectivity a suitable indicator of the lattice temperature. Error bars represent the standard deviation of the averaged signal before $\Delta t < 0$ ($\Delta t = 13$ ns).



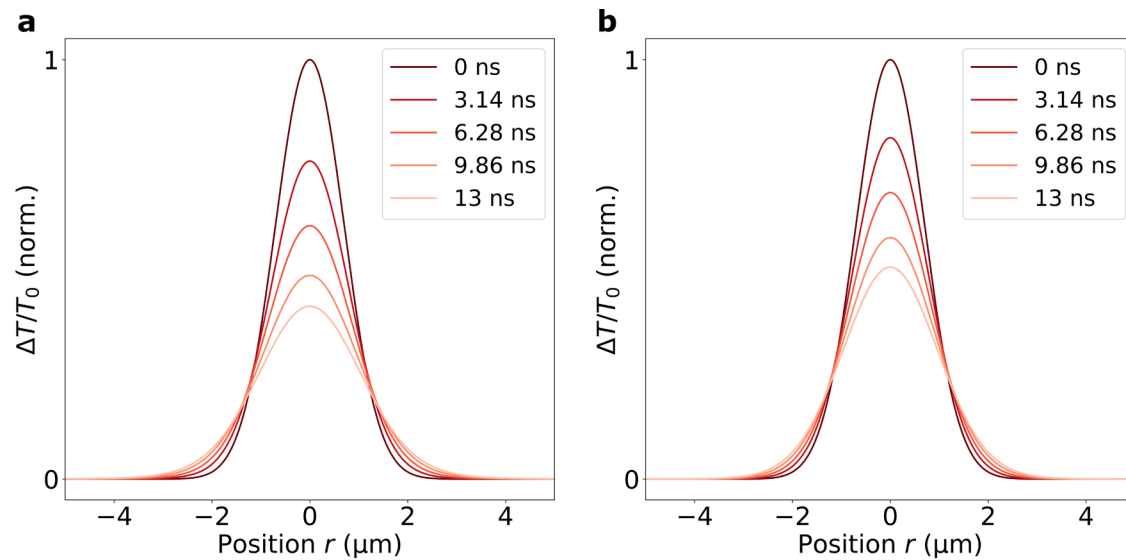
Extended Data Fig. 6 | Fluence dependent spatial scans. **a–b**, In-phase (a) and out-of-phase (b) signals (in volts, V) obtained from an 8-layer MoSe₂ sample at different pump fluences. **c–d**, Normalized profiles, whose nearly identical shapes confirm that we are operating in the linear regime and that the transient reflectivity profile is a suitable indicator of the lattice temperature profile. **e–f**, In-

phase (e) and out-of-phase (f) signals (in volts, V) obtained from a 3-layer MoSe₂ sample at different probe fluences. **g–h**, Normalized profiles, whose nearly identical shapes indicate that there are no undesired effects of our probe light on the spatial profiles.



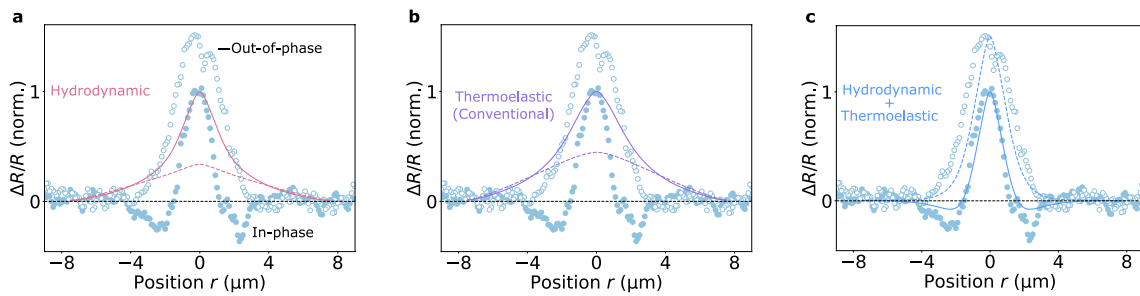
Extended Data Fig. 7 | Experimentally obtained spatial profiles for different thicknesses. a–h, In-phase (filled markers) and out-of-phase (open markers) spatial profiles measured on suspended MoSe_2 of varying thicknesses, from 3 (a) layers to 20 (h) layers. The datasets are described by the heat diffusion

equation based on the Fourier model incorporating lock-in operation (solid line for in-phase, dashed line for out-of-phase). The out-of-phase profiles are multiplied by -1 . The obtained (effective) diffusivities are plotted in Fig. 2d.



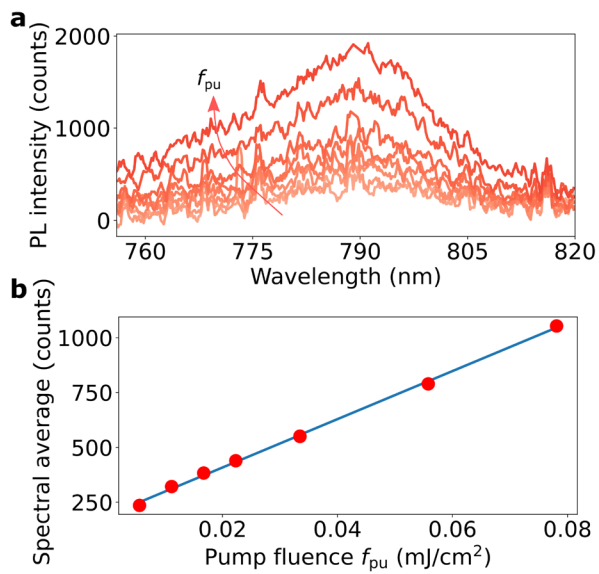
Extended Data Fig. 8 | Calculated temperature profiles from LBTE. a–b, Temperature profiles obtained via solutions to the LBTE for monolayer MoSe_2 with an initial Gaussian heat impulse of $\sigma = 0.7 \mu\text{m}$ at $T = 300 \text{ K}$ for (a) NC-PBE and (b) US-PBESOL pseudopotentials. Fitting these profiles to a diffusive model yields effective diffusivities of $0.25 \text{ cm}^2/\text{s}$ for NC-PBE and $0.18 \text{ cm}^2/\text{s}$ for US-PBESOL, corresponding to 30% and 10% reductions from the diffusive-

limit monolayer value, respectively. The LBTE percentwise reductions are in reasonable agreement with the reductions observed in the Raman measurements, confirming the role of non-diffusive heat transport. The LBTE in its form here does not explain the spatiotemporal measurements, as thermoelastic effects are not included.

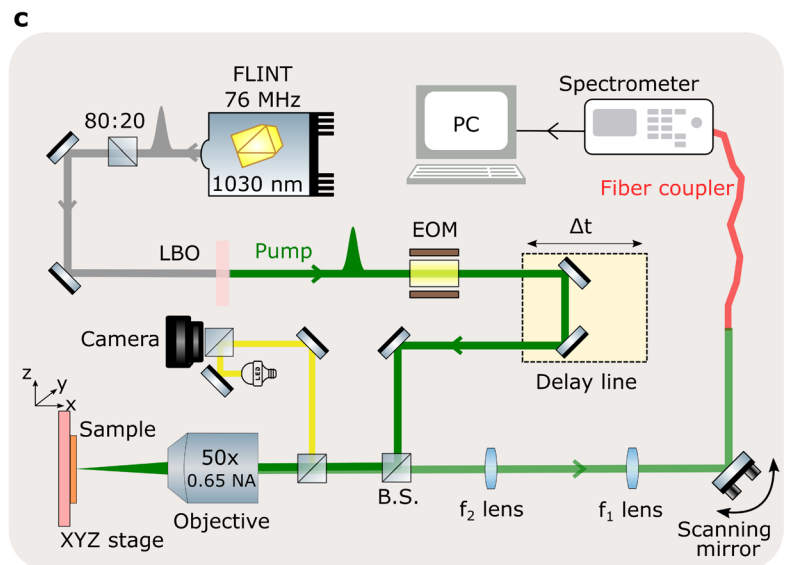


Extended Data Fig. 9 | Comparison of hydrodynamic, conventional thermoelastic, and hydro-thermoelastic models. a, Spatial profiles obtained using the hydrodynamic model describing the in-phase (solid line) and out-of-phase (dashed line) components of a monolayer MoSe₂ signal (solid circles for in-phase, open circles for out-of-phase). **b**, Corresponding profiles obtained using the conventional thermoelastic model, which considers thermal expansion and

the thermomechanical energy balance, but without including a thermoelastic heat flux contribution. **c**, Profiles from the combined hydro-thermoelastic model, which provides the best description of the experimental dataset. All profiles are normalized to the peak of the fit of the in-phase signal, and the out-of-phase profiles are multiplied by -1 .

**Extended Data Fig. 10 | Photoluminescence measurements.**

a, Photoluminescence (PL) spectra acquired from the suspended region of a monolayer MoSe₂ sample at a few different pump laser (wavelength = 515 nm) powers. **b**, Spectral average of the PL spectra at different fluences, exhibiting



a linear dependence, showing that effects of an electron–hole liquid phase can be discarded. **c**, Schematic of the PL measurement setup, which is a simple adaptation of the spatiotemporal thermometry setup.